Tunable redox activity at Fe^{3+} centers in colloidal $ATiO_3$ (A = Sr and Ba) nanocrystals

Muhammad Abdullah, Ruby J. Nelson and Kevin R. Kittilstved*

Department of Chemistry, University of Massachusetts Amherst, 710 North Pleasant Street, Amherst, Massachusetts 01003, USA

ABSTRACT: The synthesis and characterization of substitutional Fe^{3+} in sub-10 nm colloidal $SrTiO_3$ and $BaTiO_3$ nanocrystals (NCs) is reported. Significant and reversible changes to the electronic structure of the Fe-dopants in the NCs with excess n-type defects are observed by electronic absorption and electron paramagnetic resonance (EPR) spectroscopies. These n-type defects are identified as paramagnetic Ti^{3+} trap states that are created by anaerobic photodoping of colloidal suspensions with UV light in the presence of a hole scavenger. The appearance of the Ti^{3+} defects is correlated with the disappearance of the Fe^{3+} EPR signal that we attribute to the reduction of Fe^{3+} dopants to the EPR-silent Fe^{2+}. This reduction of the Fe-dopant is totally reversible upon reoxidation of the nanocrystals with air. The stabilization of Fe^{2+} in these lattices has been observed in $SrTiO_3$ and $BaTiO_3$ thin films and bulk powders after reducing the samples under extreme conditions that convert only a fraction of the Fe^{3+} dopants. In contrast, the controlled reduction of apparently every Fe^{3+} dopant to Fe^{2+} in these colloidal NCs can be achieved with just UV photons at room temperature. This work expands upon the types of reversible interactions that can exist between aliovalent magnetic dopants and charge carriers in d^0-based metal oxide semiconductors.

Exploiting the properties of semiconductor nanomaterials by incorporating impurities constitutes a long-standing challenge to materials chemistry that has hindered their implementation in various technologies.[1-4] Numerous studies have focused on the design of high-quality colloidal nanocrystals (NCs) with controlled incorporation of either aliovalent dopants to tune the carrier concentration or magnetic dopants for spin-based electronic or quantum information processing applications.[5-8] Significant progress has occurred in recent years with respect to introducing excess charge carriers into metal oxide semiconductors through aliovalent doping,[9-10] control over material stoichiometry,[11-12] photochemical (also known as photodoping),[13-14] doping via electron transfer from a chemical reductant,[15] and electrochemical doping.[16]

An emerging class of substitutional dopants that function simultaneously as aliovalent dopants and paramagnets has received much attention due to their multifunctionality. Examples of such dopants in oxide semiconductors are Fe^{3+}-doped ZnO (Fe^{3+}:ZnO),[10,17] where Fe^{3+} dopant acts as an electron donor, and Cr^{3+}:$SrTiO_3$ where Cr^{3+} substitutes at the Ti^{4+} site and behaves as an acceptor.[18-19] The aliovalent magnetic dopants of relevance to our studies are the 3d transition metal ions in Ti-based oxide semiconductors. $SrTiO_3$ is a wide-gap semiconductor with the bottom of the conduction band having primarily empty Ti-3d character. This electronic structure feature is common with so-called d^0 semiconductors and can be exploited to produce quasi-delocalized Ti^{3+} defect centers (self-trapped electrons) after an increase in carrier concentration.[15,20] Magnetic ordering has also been reported in Ti-based oxide semiconductors containing aliovalent magnetic dopants including Cr^{3+}:TiO_2, Co^{2+}:TiO_2, Fe:$SrTiO_{3-\delta}$, and Co^{2+}:(La,Sr)TiO_3.[21-24]

We recently reported that the spin relaxation time of Cr^{3+} dopants in colloidal $SrTiO_3$ NCs is accelerated by the presence of photochemically-introduced Ti^{3+} defects.[25] We demonstrated an apparent enhancement of this effect specifically in the Cr^{3+}:$SrTiO_3$ NCs, relative to the Cr^{3+}-doped bulk powders.[15] The discovery of this efficient and reversible control over the spin-relaxation time of localized Cr^{3+} motivated our current work to explore the behavior of additional aliovalent magnetic dopants in d^0 semiconductor NCs. Herein we report the preparation of sub-10 nm Fe-doped $SrTiO_3$ and $BaTiO_3$ colloidal NCs using hydrothermal methods described previously by our group.[26-27] We confirm that the Fe is in Fe^{3+} state and is located at the octahedral Ti^{4+} sites in as-prepared NCs by electron paramagnetic resonance (EPR) spectroscopy. Upon anaerobic photodoping of colloidal NCs, the EPR signal of Fe^{3+} disappears with increasing Ti^{3+} concentration. The lack of Fe^{3+} EPR signal in the photodoped $SrTiO_3$ and $BaTiO_3$ persists down to 100 K, where the Ti^{3+} EPR signal is observed. These results are consistent with the electrons trapping at the Fe^{3+} sites prior to accumulating at Ti^{3+} defects in these NCs. This electron trapping phenomenon reduces Fe^{3+} to EPR-silent Fe^{2+} centers and can be effectively manipulated as a function of irradiation time. All of the spectroscopic changes induced by photodoping are fully reversible upon aerobic oxidation of the photodoped sample.

METHODS AND MATERIALS

Materials:

Strontium hydroxide octahydrate ($Sr(OH)_2{\cdot}8H_2O$, 99%, Alfa Aesar), barium hydroxide octahydrate ($Ba(OH)_2{\cdot}8H_2O$, 99%, Alfa Aesar), titanium(IV) bis(ammonium lactate) hydroxide (TALH, 50% in water, Alfa Aesar), tetramethylammonium hydroxide (NMe_4OH, Acros Organics), sodium hydroxide (NaOH, Certified ACS, Fisher Chemical), hydrazine hydrate ($N_2H_4{\cdot}H_2O$, 99%, Acros Organics), oleylamine (>50%, TCI America), oleic acid (>95%, Fisher Chemical), iron nitrate nonahydrate ($Fe(NO_3)_3{\cdot}9H_2O$, 99.99% Sigma Aldrich), ethanol (200 proof, PHARMCO-AAPER),

QC-21 elements standard (PerkinElmer, 5% HNO_3), nitric acid (Certified ACS Plus, Fisher Chemical), hydrochloric acid (Certified ACS Plus, Fisher Chemical), toluene (Optima, Fisher Chemicals) and hexanes (Optima, Fisher Chemicals) were all used as received.

Synthesis of Nanocrystals:

Pure and Fe-doped $SrTiO_3$ colloidal NCs. Synthesis of colloidal $SrTiO_3$ NCs was carried out by a modified hydrothermal method reported earlier by Harrigan *et al.*[26] In a typical synthesis, 1.25 mmol of TALH and 1.25 mmol of $Sr(OH)_2{\cdot}8H_2O$ were dissolved in 30 mL of distilled water. The pH of the solution was then adjusted to 12.1 with an aqueous solution of NMe_4OH (10 M) followed by the addition of oleic acid (2.5 mmol) and hydrazine (5 mmol). The resulting solution was transferred to a 45 mL Teflon-lined autoclave (4744 General Purpose Acid Digestion Vessel, Parr Instrument Company) and heated to 200 °C in an oven for 24 hours. The resulting NCs were collected, washed with ethanol several times, suspended in hexanes, and sonicated for about 30 minutes to produce a cloudy suspension. Finally, a transparent hexane layer containing NCs was extracted by centrifuging the cloudy suspension (5 min at 4000 rpm). These NCs can be further purified by precipitation with ethanol. Synthesis of nominally 0.5% Fe-doped $SrTiO_3$ NCs was carried out by adding 625 μL of 0.01 M aqueous solution of $Fe(NO_3)_3{\cdot}9H_2O$ right after adjusting the pH of the precursor solution. Similarly, nominally 1% Fe-doped $SrTiO_3$ NCs were prepared by adding 1.25 mL of 0.01 M aqueous solution of $Fe(NO_3)_3{\cdot}9H_2O$.

Pure and Fe-doped $BaTiO_3$ colloidal NCs. Synthesis of $BaTiO_3$ NCs was carried out by a similar hydrothermal method but included constant magnetic stirring.[27] In a typical synthesis, 1.5 mmol of each of TALH and $Ba(OH)_2$ were dissolved in 24 mL distilled water followed by 6 mL of 5 M NaOH aqueous solution. The reaction mixture was then transferred to a 45 mL Teflon-lined autoclave, and oleylamine (6 mmol), oleic acid (6 mmol), and hydrazine (6 mmol) were added. The sealed autoclave was placed in custom-made aluminum block housing heated to 215 °C and stirred continuously for 24 hours using a stirring hotplate. After the synthesis, the autoclave was cooled down to room temperature, and the crude product was collected along with water into two separate test tubes and washed with ethanol (33% by volume) twice. The solid product was then dissolved in hexanes to produce a cloudy suspension with sonication (15 minutes). Finally, the hexane layer containing the NCs was extracted by centrifuging the suspension. Synthesis of nominally 0.5% Fe-doped $BaTiO_3$ NCs was carried out by adding 750 μL of 0.01 M aqueous solution of $Fe(NO_3)_3{\cdot}9H_2O$ before adding NaOH.

Physical characterization:

All measurements presented below were collected on either pure or 0.5% Fe-doped $SrTiO_3$ NCs (referred to as Fe:$SrTiO_3$ hereafter) and pure or 0.5% Fe-doped $BaTiO_3$ NCs (referred to as Fe:$BaTiO_3$ hereafter) unless specified otherwise. Electronic absorption and emission spectra were collected at room-temperature on colloidal NCs in air-tight quartz cuvette on Cary 50 Bio and Cary Eclipse, respectively. Near-IR absorption measurements were collected on Varian 670 FT spectrometer equipped with an InGaAs detector and near-IR quartz beam splitter using a 1-mm pathlength quartz cuvette. The functional groups and surface chemistry analysis of solvent-free NCs were carried out on a Bruker Alpha-P FTIR spectrophotometer equipped with an attenuated total reflectance (ATR) platinum diamond optic. EPR measurements were carried out on continuous wave (CW) Bruker Elexsys-500 fitted with Super High QE X-band cavity (ER4123SHQE) and cryostat (ESR-900, Oxford) for low-temperature measurements. For the photodoping experiments, a 75 W xenon lamp was used (60000 Q series, Oriel Corporation). Transmission electron microscopy (TEM, JEOL 2000FX) images were measured from freshly prepared NCs drop-casted onto carbon-coated (3nm) copper grids (CF400-CU-50, Electron Microscopy Sciences). The average size distribution and standard deviation were generated by analyzing a few hundred particles from TEM images using ImageJ software. Powder X-ray diffraction patterns were collected in a Bragg-Brentano configuration and Cu K-source (Rigaku Smart Lab SE). Metal ion stoichiometry was measured on dissolved ensembles of NCs and measured by inductively coupled plasma - optical emission spectrometer (ICP-OES, Perkin Elmer Optima 4300 DV).

Photodoping:

Photodoping experiments were performed to introduce excess electrons in as-prepared NCs. Sample preparation was completed in the argon-filled glove box where NCs suspended in hexanes were transferred to a 1 cm air-tight cuvette before removal. Samples were photodoped by prolonged exposure to unfocused irradiation from 75 W xenon lamp in the presence of EtOH (0.5 mL, >100 eq/NC) as a sacrificial reductant. The electronic absorption spectra were taken periodically during the entire photodoping process. It was estimated that the NCs were photodoped to their saturation limit when no further spectroscopic changes could be observed following prolonged exposure. For in-situ EPR measurements, NCs were transferred to a 4-mm air-free EPR tube, and photodoping procedure inside the EPR resonator was carried out by UV irradiation via fiber optics. The lamp was warmed up 30 min before each photodoping experiment in order to achieve uniform temperature and irradiation intensity.

RESULTS AND DISCUSSION

The crystallinity and phase purity of as-prepared undoped and Fe-doped $SrTiO_3$ NCs were confirmed by powder X-ray diffraction measurements (see Figure S1). The diffraction patterns of the both samples are indexed to cubic $SrTiO_3$ (space group: $Pm\bar{3}m$) with no additional secondary phases.[28] A slight increase of the lattice parameter was observed in the Fe:$SrTiO_3$ NCs. This typical lattice expansion is attributed to the substitution of a relatively larger Fe^{3+} ion (0.79 Å) at the Ti^{4+} (0.74 Å) sites and is consistent with other spectroscopic evidence of Fe^{3+} substitution shown below.[29-30] TEM images also confirmed that the as-prepared product is nanocrystalline and exhibits cubic morphology with an average edge length of 7.7 nm ± 1.9 nm in good agreement with the size calculated from the diffraction pattern (see Figure S2 and Table ST1). The elemental analysis showed a total of 1.03 % Fe content in the nominally 0.5% Fe-doped $SrTiO_3$ NCs (see Figure S3 and Table ST2). The titanium precursor (TALH) also contains small amounts of TiO_2 impurities due to slow hydrolysis at pH 8.5. The presence of such impurities thus overestimates the concentration of Ti^{4+} in the reaction solution.

Figure 1A shows the electronic absorption spectra and the corresponding color photographs of concentrated solutions of $SrTiO_3$ and Fe:$SrTiO_3$ NCs in hexanes. The absorbance at *ca.* 3.25 eV dominates the electronic absorption spectra of both the samples, consistent with the bandgap transition energy of $SrTiO_3$.[31] Fe:$SrTiO_3$ NCs exhibit an additional broad sub-bandgap absorption that tails into the visible region that is responsible for the yellowish-brown color of the concentrated suspensions (see photographs in

Figure 1A insets). This absorption tail was previously observed in bulk Fe:$SrTiO_3$ involving deep Fe^{3+} impurity levels and explicitly attributed to a valence band-to-metal charge transfer transition.[32-33]

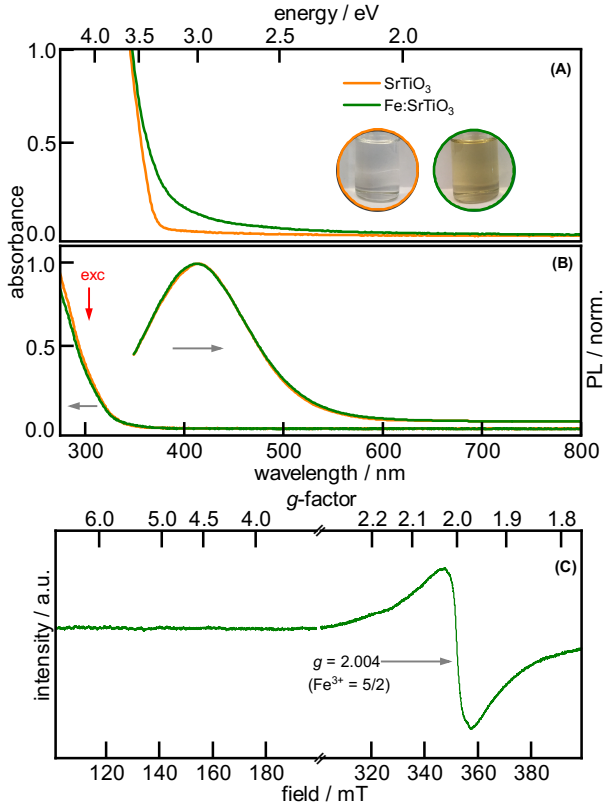

Figure 1. (A) Room temperature electronic absorption spectra and color photographs of concentrated solutions of $SrTiO_3$ (orange) and Fe:$SrTiO_3$ (green) in hexanes. (B) Absorption and PL spectra of dilute solutions of both samples excited at 300 nm. The left axis represents the optical density of dilute solutions that is ≤0.5 at the excitation wavelength, while that normalized PL intensity is displayed on the right axis. (C) Room temperature EPR spectrum of as-prepared Fe:$SrTiO_3$ NCs showing a single, broad resonance at ~350 mT (g = 2.004).

Figure 1B displays the electronic absorption and photoluminescence (PL) spectra of dilute suspensions of $SrTiO_3$ and Fe:$SrTiO_3$ NCs excited at 300 nm. The normalized PL spectra of both the samples appear identical, with a broad emission feature centered around ~3.0 eV. This PL energy is in agreement with the previously reported emission described as self-trapped excitons' (STE) recombination at the surface of $SrTiO_3$.[34-35] There is no discernable variance between the PL energy of $SrTiO_3$ and Fe:$SrTiO_3$ NCs. This observation suggests that both the samples possess similar surface chemistry and that radiative recombination from the STE state is faster than the energy transfer to Fe-centered excited states. FTIR measurements were also utilized on solvent evaporated NCs (see Figure S4) to understand the surface coordination environment. The FTIR spectra display the characteristic symmetric and asymmetric carboxylate stretches (doublet at 1540 cm^{-1} and 1450 cm^{-1}) and aliphatic bands around 2900 cm^{-1} that are consistent with oleate passivation of the NC surface.

To probe the local environment of Fe^{3+} dopants in as-prepared Fe:$SrTiO_3$ NCs, we employed conventional X-band EPR spectroscopy, which is well-reported to replace octahedral Ti^{4+} in $SrTiO_3$ lattice.[36-37] For Fe^{3+} ($3d^5$) in an environment of cubic symmetry (ground state term $^6A_{1g}$), the spin degeneracy can only be lifted by a magnetic field, thus making Fe^{3+} a suitable dopant for investigation by EPR spectroscopy. Figure 1C shows the room temperature EPR spectrum of Fe:$SrTiO_3$ NCs. The broad isotropic resonance at ~350 mT (g = 2.004) corresponds to high-spin Fe^{3+} electronic states at the octahedral site in correspondence with literature.[38-40] No evidence of pseudo-octahedral Fe^{3+} at the $SrTiO_3$ NC surface was detected in the low-field region.

We previously showed that both the spin-lattice (T_1) and spin-spin (T_2) relaxation times of Cr^{3+} ions in Cr-doped $SrTiO_3$ colloidal NCs could be effectively accelerated by the presence of fast-relaxing paramagnetic Ti^{3+} defects.[25] To probe the interaction between excess electrons and substitutional Fe^{3+}, we performed photodoping experiments on Fe:$SrTiO_3$ NCs. A detailed procedure for introducing excess electrons via photodoping is described in the experimental section. Briefly, UV irradiation of an anaerobic solution of as-prepared NCs creates electron/hole pairs (excitons) followed by the rapid quenching of holes with ethanol which leaves excess electrons in NCs.

Figure 2 shows the electronic absorption spectra of Fe:$SrTiO_3$ NCs as a function of photodoping time. The absorption spectrum of as-prepared NCs is dominated by $SrTiO_3$ bandgap transition above ~3.25 eV. With increased photodoping time, a new absorption feature extending throughout the entire visible region and centered at ~1.5 eV (900 nm) appears, and the physical appearance of the sample changes to dark blue (see Figure 2 insets). This broad near-IR transition is assigned to the metal-to-metal charge transfer (MMCT) transition from localized Ti^{3+} sites to the conduction band reported previously in photodoped Cr-doped $SrTiO_3$ and TiO_2.[25,41] The only change in the electronic absorption spectrum with increasing photodoping time is the growth of this MMCT transition. We have no evidence that photodoping creates delocalized electrons in the conduction band (e^-_{CB}). Recent reports showed that n-type doping of small anatase TiO_2 NCs can lead to accumulation of e^-_{CB} as observed spectroscopically by significant blue-shifts in the band-edge energy from the Moss-Burstein effect and formation of a localized surface plasmon resonance (LSPR) in the mid-IR region.[5] Milliron reported similar spectroscopic changes caused by e^-_{CB} accumulation in Nb^{5+}-doped TiO_2 NCs.[6,42] The lack of absorption in the mid-IR region further confirms that e^-_{CB} are absent in our photodoped $SrTiO_3$ NCs (see Figure S5).

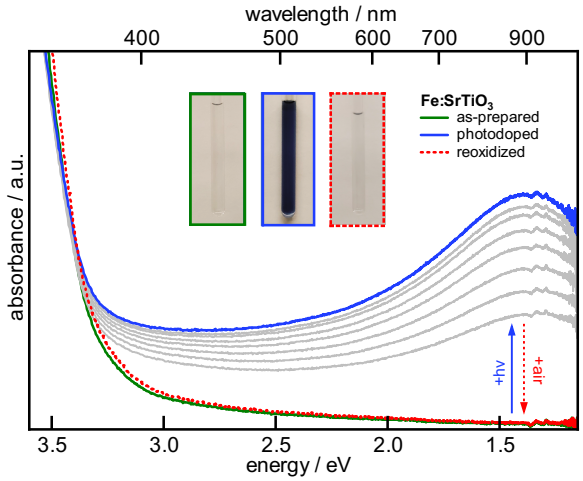

Figure 2. Electronic absorption spectra of an air-free solution of Fe:$SrTiO_3$ NCs in hexanes as a function of photodoping time. The green spectrum corresponds to as-prepared NCs. The intermediate grey lines show the data collected at various stages of photo-irradiation in the

presence of EtOH. The blue spectrum belongs to maximally photodoped NCs, and the dotted red line overlapping the as-prepared data represents the reoxidized NCs upon opening the sample to air. The color photographs for as-prepared, photodoped, and reoxidized NCs are shown in insets.

EPR spectroscopy was also utilized to monitor any associated changes in substitutional Fe^{3+} with the concomitant occurrence of Ti^{3+} ($3d^1$, $^2T_{2g}$ ground term) throughout the photodoping duration. Figure 3A shows the room temperature EPR spectra of Fe:$SrTiO_3$ NCs collected before and after photodoping. As shown in Figure 1C, the EPR spectrum of as-prepared Fe:$SrTiO_3$ NCs (green) exhibits only a single, broad resonance at $g = 2.004$ assigned to substitutional Fe^{3+} ions. However, after photodoping for 20 min, the Fe^{3+} signal completely disappears, and a new signal at ~355 mT ($g = 1.94$) is detected that is attributed to the formation of paramagnetic Ti^{3+} consistent with absorption measurements shown in Figure 2. The Ti^{3+} EPR signal in photodoped $SrTiO_3$ NCs is nearly isotropic. The disappearance of the Fe^{3+} signal and the simultaneous emergence of Ti^{3+} in the photodoped Fe:$SrTiO_3$ samples are entirely reversible processes. The above-mentioned spectroscopic changes were quantitatively recovered by exposing the photodoped sample to air, as shown by the red dotted spectra in Figures 2 and 3.

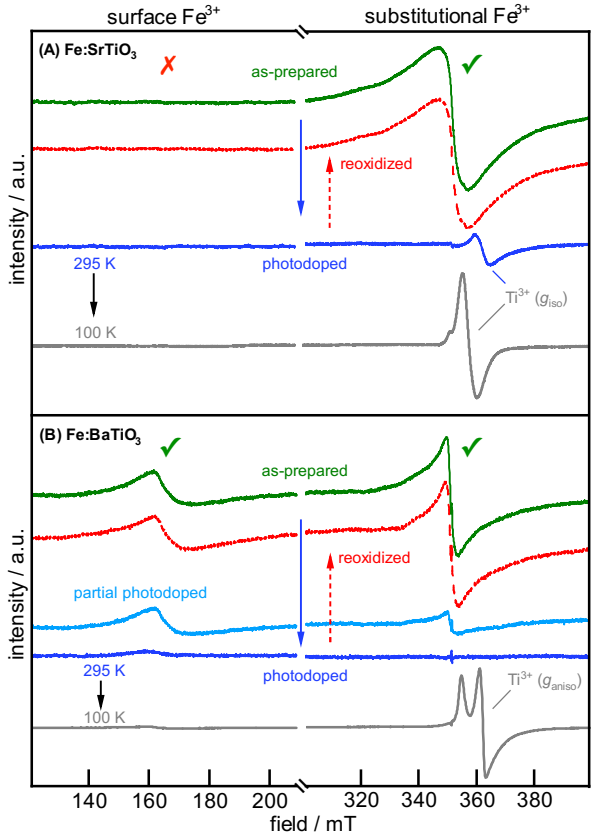

Figure 3. Room-temperature and cryogenic EPR spectra of an air-free solution of (A) Fe:$SrTiO_3$ and (B) Fe:$BaTiO_3$ NCs in hexanes. The green spectra in both samples correspond to as-prepared NCs, and the blue spectra denote the photodoped NCs. The dotted red lines overlapping the as-prepared data represent the reoxidized NCs upon opening the samples to air.

These observations are similar to our recent report on Cr^{3+}-doped $SrTiO_3$ NCs, where photodoping results in the disappearance of the Cr^{3+} EPR signal at room temperature.[25] The Cr^{3+} signal in that study reappeared after lowering the sample temperature to slow down the accelerated spin-relaxation. However, the EPR spectrum of photodoped Fe:$SrTiO_3$ NCs collected at 90 K (Figure 4) indicates a permanent elimination of Fe^{3+} signal even at the cryogenic temperature. This observation suggests that Fe^{3+} may not have any spin-interactions with Ti^{3+} defects, unlike Cr^{3+} in photodoped $SrTiO_3$ NCs. The change in spin relaxation is caused by the near-resonant cross-relaxation phenomenon between Ti^{3+} and Cr^{3+} with similar *g*-values (Ti^{3+}:1.945, Cr^{3+}:1.978).[43-44] We speculate that the Fe^{3+} signal at a much higher *g*-value (2.004) can make the spin cross-relaxation process with Ti^{3+} defects non-resonant and, therefore, less effective.

The observation of total disappearance of the Fe^{3+} signal in the $SrTiO_3$ NCs is consistent with at least some, if not all, of the substitutional Fe^{3+} dopants being reduced to EPR-silent Fe^{2+} dopants. This observation is also similar to our recent results on n-type Fe-doped ZnO NCs.[9,45-46] To probe the relative positions of the $Fe^{3+/2+}$ and Ti^{3+} energy levels in $SrTiO_3$ bandgap, we performed *in-situ* photodoping experiments (see Figure S6). The sequential disappearance of the Fe^{3+} EPR signal within a few seconds of photodoping followed by the appearance of the Ti^{3+} signal suggests (a) there is a gradual rise in Fermi level and (b) that the $Fe^{3+/2+}$ redox level is situated deeper than the Ti^{3+} level. Scheme 1 illustrates the proposed mechanism of electron trapping in Fe:$SrTiO_3$ NCs. The photoexcitation of charge carriers followed by rapid hole quenching with EtOH raises the Fermi level below the conduction band, which results in the reduction of substitutional Fe^{3+} to Fe^{2+} prior to self-trapping at the Ti^{3+} defects. Upon exposing the photodoped sample to air, these changes are then reversed, and Fe^{3+} is quantitatively recovered.

Scheme 1. A schematic representation of reversible electron trapping at $Fe^{3+/2+}$ redox level in photodoped Fe:$ATiO_3$ NCs.

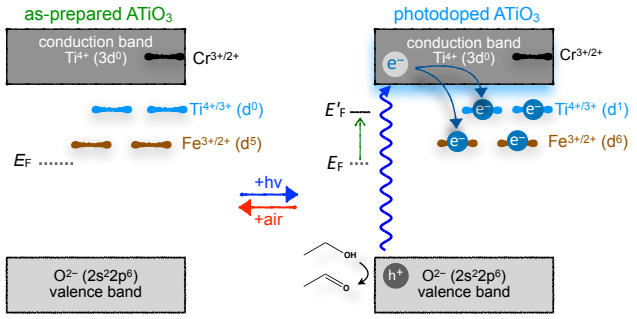

To validate the generality of this reversible electron trapping, we extended the study to Fe^{3+}-doped $BaTiO_3$ colloidal NCs prepared from a similar hydrothermal method (see Figure S7 and Table ST3). Electronic absorption spectra of photodoped NCs of $BaTiO_3$ and Fe:$BaTiO_3$ show a similar but slightly blue-shifted broad absorption feature observed in photodoped $SrTiO_3$ NCs (see Figure S8). The EPR spectrum of as-prepared Fe:$BaTiO_3$ NCs is shown in Figure 3B and is similar to the spectrum of Fe:$SrTiO_3$ but also displays an additional intense broad signal at ~160 mT ($g = 4.23$). This feature increases in relative intensity compared to the substitutional Fe^{3+} signal and is observed in nominally 1% Fe:$SrTiO_3$ NCs (see Figure S9). This feature at $g = 4.23$ is attributed to a fraction of Fe^{3+} dopants located near the surface of NCs with pseudo-octahedral symmetry. We attribute the higher relative intensity of this surface Fe^{3+} EPR signal to the smaller size of $BaTiO_3$ (~5 nm) that results in a larger fraction of Fe^{3+} dopants either on the surface or in near-surface sites compared to $SrTiO_3$ NCs (~8 nm). These surface Fe^{3+} sites have variation in the coordinating ligands on the $SrTiO_3$ and $BaTiO_3$ NC

surfaces. The alkylamine surface ligands used during the synthesis of the Fe:$BaTiO_3$ NCs are also known to remove surface Fe^{3+} dopants as observed in a post-synthetic ligand exchange process in Fe^{3+}:ZnO NCs.[10]

Further support for the distinction between surface and substitutional Fe^{3+} in the $BaTiO_3$ NCs is based on a comparison of the spectral changes of this low-symmetry surface Fe^{3+} and substitutional Fe^{3+} at g = 2.004 as a function of photodoping time (see Figure 3B). Initially, the EPR signal for substitutional Fe^{3+} is more intense than the surface Fe^{3+}; however, after photodoping for a short time (~5 min), the relative EPR signal intensities flip. Further photodoping leads to the complete disappearance of the substitutional Fe^{3+} with some residual surface Fe^{3+} signal still observed albeit weaker. The EPR spectrum of the photodoped Fe:$BaTiO_3$ NCs collected at 100 K also shows an anisotropic Ti^{3+} defect signal centered around ~355 mT as shown in Figure 3B.. The anisotropy of the g-values observed for the Ti^{3+}-related defect in photodoped colloidal Fe:$BaTiO_3$ NCs presented here ($g_{x,y}$ = 1.94, g_z = 1.97) is exactly opposite to that reported in bulk $BaTiO_3$ powders and single crystals ($g_{x,y}$ = 1.97, g_z = 1.94).[47] Both $SrTiO_3$ and $BaTiO_3$ NCs possess cubic structures by powder XRD. Therefore, the crystal field surrounding a self-trapped electron at the B-site (Ti^{3+}) should be isotropic; however, Ti^{3+} is Jahn-Teller active and will distort to axial symmetry in both photodoped $SrTiO_3$ and $BaTiO_3$ albeit to varying extents.[48] The likelihood of Ti^{3+} defects being near or at the NC surface in the smaller $BaTiO_3$ NCs would also lead to distortion of the Ti^{3+} EPR signal due to mixed coordination with the lattice and surface ligands that adds a rhombic component to the g-anisotropy. The anisotropic lineshape is less resolved in the photodoped $SrTiO_3$ and Fe:$SrTiO_3$ NCs and may be the result of the larger average particle size.

The existence of both axial and rhombic EPR signals associated with two distinct Ti^{3+} centers in thermal equilibrium was recently reported in photodoped TiO_2 nanoparticles.[49] This observation is unique to photodoped TiO_2 nanoparticles and has not been observed in the bulk. We postulate that the variation of the Ti^{3+} EPR signals in photodoped Fe:$SrTiO_3$ and Fe:$SrTiO_3$ NCs compared to the bulk n-type $BaTiO_3$ and Fe:$SrTiO_3$ is caused by differences in (1) the microenvironment surrounding the Ti^{3+} center and (2) its proximity to the NC surface. We are currently investigating the microscopic origins of the EPR signal in photodoped d^0 semiconductor NCs. Nevertheless, there is no evidence of Fe^{3+} in photodoped Fe:$BaTiO_3$ NCs, which is consistent with our proposed model of electron trapping on Fe^{3+} in $SrTiO_3$ NCs. The drastic decrease in substitutional Fe^{3+} before surface Fe^{3+} suggests that the former is situated deeper than surface $Fe^{3+/2+}$ redox level in $BaTiO_3$ NCs or that electronic coupling between surface Fe^{3+} and the self-trapped Ti^{3+} defects is weaker. Similar step-wise reductions were also observed in the recent report on n-type Fe^{3+}:ZnO NCs containing both substitutional and surface Fe^{3+} species.[9,46] Suzuki *et al.* have reported that the $Fe^{3+/2+}$ redox level is located ~0.7-0.8 eV below the conduction band minimum in $BaTiO_3$ single crystals, while in $SrTiO_3$ the $Fe^{3+/2+}$ level is nearly degenerate with the conduction band.[50] Our results are consistent with the $Fe^{3+/2+}$ energy level lying at a more positive potential than the conduction band and Ti^{3+} level in both $SrTiO_3$ and $BaTiO_3$ NCs.

Several other reports show that at least some of the Fe^{3+} can be reduced to Fe^{2+} in $SrTiO_3$ and $BaTiO_3$ bulk powder and thin films under reducing conditions.[51-53] However, most of these reductions are limited to the surface and sub-surface Fe dopants and typically require elevated temperatures. Stabilization of Fe^{2+} in reduced $SrTiO_3$ and $BaTiO_3$ is also challenging as it requires additional charge compensation that could include the formation of oxygen vacancies.[54] The requirement of oxygen vacancies and effect on the lattice may be responsible for the reduction of only some of the Fe^{3+} dopants in bulk $ATiO_3$. In contrast, the charge compensation during photodoping is accomplished by proton (H^+) adsorption at the surfaces as reported in TiO_2 and other oxide NCs.[14,55] Furthermore, photodoping can be achieved at room temperature with just UV photons and a sacrificial hole scavenger. This facile method offers a controlled and reversible reduction of every Fe^{3+} dopant throughout the entire $ATiO_3$ NC.

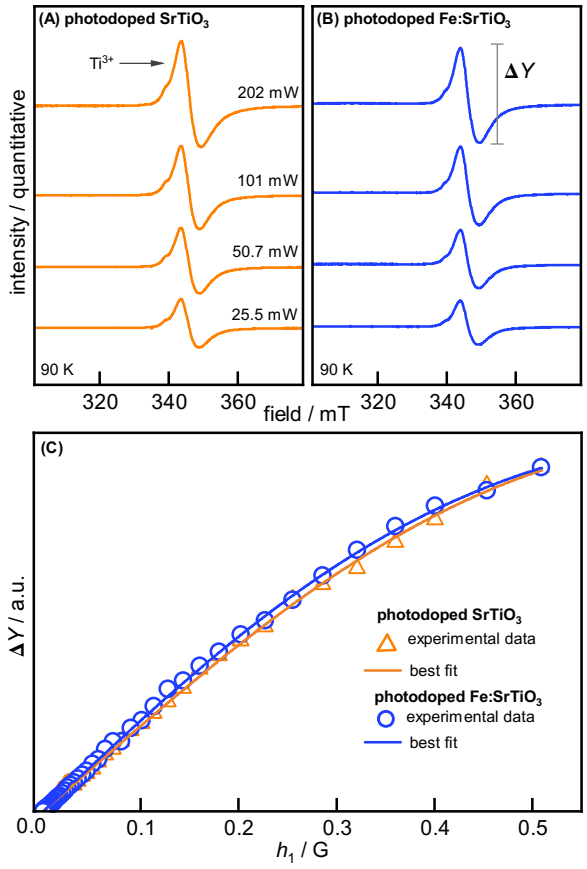

Figure 4. Representative CW-EPR spectra of maximally photodoped (A) $SrTiO_3$ and (B) Fe:$SrTiO_3$ NCs at 90 K at selected microwave powers. The signal intensity defined as ΔY and best fits to equation 2 (see Figure S3 and Table S2) for each measurement plotted as a function of microwave power (h_1) is shown in the bottom panel (C).

These results provide sufficient evidence that photochemically-introduced n-type carriers reduce the Fe^{3+} dopants to EPR-silent Fe^{2+} ions, in contrast to the acceleration of spin-relaxation time of Cr^{3+} dopants.[25] However, they do not rule out the possible cross-relaxation between Fe^{3+} and Fe^{2+} or Ti^{3+} and Fe^{2+} centers in photodoped $ATiO_3$ NCs. High-field EPR measurements to directly observe Fe^{2+} dopants are planned. However, with X-band CW-EPR, we were able to study the effect of Fe^{2+} on Ti^{3+} spin-dynamics. To probe this, we performed power saturation rollover experiments and linewidth analysis of Ti^{3+} signal in the absence and presence of Fe^{2+}. These experiments were performed on photodoped $SrTiO_3$ (no Fe^{2+}) and Fe:$SrTiO_3$ (Fe^{3+} fully reduced to Fe^{2+}) at 90 K (See Figures 4A-C, S10-11 and Table ST4). No significant difference in saturation rollover behavior orT_2 time of the Ti^{3+} defects in both photodoped $SrTiO_3$ (2.65 ± 0.06 ns) and photodoped Fe:$SrTiO_3$

(2.50 ± 0.04 ns) was observed. The slight difference in T_2 can be attributed to variation in average Ti^{3+} concentrations in the photodoped NCs. These results suggest that the spin properties of Ti^{3+} defects are not affected by the presence of Fe^{2+} dopants in photodoped $SrTiO_3$ NCs.

CONCLUSIONS

We presented synthesis and characterization of Fe-doped $SrTiO_3$ and $BaTiO_3$ colloidal NCs and investigated their dopant-defect interaction using various spectroscopies. The results presented here provide convincing evidence that the valance state of Fe dopant can be modulated between 3+ and 2+ by post-synthetic manipulation of carrier densities in these NCs. The introduction of excess charge carriers at room temperature using photodoping methods into Fe^{3+}:$SrTiO_3$ and Fe^{3+}:$BaTiO_3$ colloidal NCs results in the reduction of Fe^{3+} to Fe^{2+}. This electron storage capacity of both the dopant and lattice makes these colloidal NCs potentially suitable for non-aqueous redox flow batteries. Direct verification of Fe^{2+} is challenging due to the air-sensitive nature of the photodoped NCs. We are currently investigating alternative methods to achieve air-stable n-type defects in Fe-doped $ATiO_3$ and related d^0 colloidal semiconductor NCs.

ASSOCIATED CONTENT

Supporting Information

The Supporting Information is available free of charge on the ACS Publications website.

Additional characterization and analysis (PDF)

AUTHOR INFORMATION

Corresponding Author

*Kevin R. Kittilstved. Email: kittilstved@chem.umass.edu

Author Contributions

The manuscript was written through the contributions of all authors.

Funding Sources

This work was supported by the National Science Foundation (DMR-1747593). The acquisition of the powder X-ray diffractometer used in this work was supported by the National Science Foundation Major Research Instrumentation program (CHE-1726578). R.J.N was supported by the National Science Foundation Research Experience for Undergraduates program (CHE-1659266).

Notes

The authors declare no competing financial interest.

ACKNOWLEDGMENT

We thank Prof. Dhandapani Venkataraman for access to the FTIR spectrophotometer. We acknowledge the assistance of Jillian Denhardt in ICP-OES analysis, and Dr. William Harrigan, Dr. Fumitoshi Kato and Haneen Mansoor for their valuable insight into this study.

REFERENCES

(1) Mocatta, D.; Cohen, G.; Schattner, J.; Millo, O.; Rabani, E.; Banin, U., Heavily doped semiconductor nanocrystal quantum dots. *Science* **2011**, *332*, 77-81.

(2) Queisser, H. J.; Haller, E. E., Defects in semiconductors: some fatal, some vital. *Science* **1998**, *281*, 945-950.

(3) Ohno, H., A window on the future of spintronics. *Nat. Mater.* **2010**, *9*, 952-954.

(4) Han, W.; Kawakami, R. K.; Gmitra, M.; Fabian, J., Graphene spintronics. *Nat. Nanotech.* **2014**, *9*, 794-807.

(5) Cao, S.; Zhang, S.; Zhang, T.; Fisher, A.; Lee, J. Y., Metal-doped TiO_2 colloidal nanocrystals with broadly tunable plasmon resonance absorption. *J. Mater. Chem. C* **2018**, *6*, 4007-4014.

(6) De Trizio, L.; Buonsanti, R.; Schimpf, A. M.; Llordes, A.; Gamelin, D. R.; Simonutti, R.; Milliron, D. J., Nb-doped colloidal TiO_2 nanocrystals with tunable infrared absorption. *Chem. Mater.* **2013**, *25*, 3383-3390.

(7) Shah, J.; Kotnala, R. K., Induced magnetism and magnetoelectric coupling in ferroelectric $BaTiO_3$ by Cr-doping synthesized by a facile chemical route. *J. Mater. Chem. A* **2013**, *1*, 8601-8608.

(8) Norberg, N. S.; Kittilstved, K. R.; Amonette, J. E.; Kukkadapu, R. K.; Schwartz, D. A.; Gamelin, D. R., Synthesis of colloidal Mn^{2+}:ZnO quantum dots and high-T_C ferromagnetic nanocrystalline thin films. *J. Am. Chem. Soc.* **2004**, *126*, 9387-9398.

(9) Buz, E.; Zhou, D. M.; Kittilstved, K. R., Air-stable n-type Fe-doped ZnO colloidal nanocrystals. *J. Chem. Phys.* **2019**, *151*, 134702.

(10) Zhou, D.; Kittilstved, K. R., Control over Fe^{3+} speciation in colloidal ZnO nanocrystals. *J. Mater. Chem. C* **2015**, *3*, 4352-4358.

(11) Luther, J. M.; Jain, P. K.; Ewers, T.; Alivisatos, A. P., Localized surface plasmon resonances arising from free carriers in doped quantum dots. *Nat. Mater.* **2011**, *10*, 361-366.

(12) Manthiram, K.; Alivisatos, A. P., Tunable localized surface plasmon resonances in tungsten oxide nanocrystals. *J. Am. Chem. Soc.* **2012**, *134*, 3995-3998.

(13) Liu, W. K.; Whitaker, K. M.; Kittilstved, K. R.; Gamelin, D. R., Stable photogenerated carriers in magnetic semiconductor nanocrystals. *J. Am. Chem. Soc.* **2006**, *128*, 3910-3911.

(14) Schimpf, A. M.; Gunthardt, C. E.; Rinehart, J. D.; Mayer, J. M.; Gamelin, D. R., Controlling carrier densities in photochemically reduced colloidal ZnO nanocrystals: size dependence and role of the hole quencher. *J. Am. Chem. Soc.* **2013**, *135*, 16569-16577.

(15) Lehuta, K. A.; Kittilstved, K. R., Reversible control of the chromium valence in chemically reduced Cr-doped $SrTiO_3$ bulk powders. *Dalton Trans.* **2016**, *45*, 10034-10041.

(16) Wang, C.; Shim, M.; Guyot-Sionnest, P., Electrochromic nanocrystal quantum dots. *Science* **2001**, *291*, 2390-2392.

(17) Karmakar, D.; Mandal, S.; Kadam, R.; Paulose, P.; Rajarajan, A.; Nath, T. K.; Das, A. K.; Dasgupta, I.; Das, G., Ferromagnetism in Fe-doped ZnO nanocrystals: experiment and theory. *Phys. Rev. B* **2007**, *75*, 144404.

(18) Soledade, L.; Longo, E.; Leite, E.; Pontes, F.; Lanciotti Jr, F.; Campos, C.; Pizani, P.; Varela, J. A., Room-temperature photoluminescence in amorphous $SrTiO_3$–the influence of acceptor-type dopants. *Appl. Phys. A* **2002**, *75*, 629-632.

(19) Eror, N.; Balachandran, U., High-temperature defect structure of acceptor-doped strontium titanate. *J. Am. Ceram. Soc.* **1982**, *65*, 426-431.

(20) Mansoor, H.; Harrigan, W. L.; Lehuta, K. A.; Kittilstved, K. R., Reversible Control of the Mn Oxidation State in $SrTiO_3$ Bulk Powders. *Front. Chem.* **2019**, *7*, 353.

(21) Kaspar, T. C.; Droubay, T.; Shutthanandan, V.; Heald, S. M.; Wang, C. M.; McCready, D. E.; Thevuthasan, S.; Bryan, J.; Gamelin, D. R.; Kellock, A., Ferromagnetism and structure of epitaxial Cr-doped anatase TiO_2 thin films. *Phys. Rev. B* **2006**, *73*, 155327.

(22) Matsumoto, Y.; Murakami, M.; Shono, T.; Hasegawa, T.; Fukumura, T.; Kawasaki, M.; Ahmet, P.; Chikyow, T.; Koshihara, S.-y.; Koinuma, H., Room-temperature ferromagnetism in transparent transition metal-doped titanium dioxide. *Science* **2001**, *291*, 854-856.

(23) Pei, Y.; Zhang, R.; Song, Y.; Bi, J.; Xu, W.; Zhou, C.; Duan, J.; Yang, J.; Cao, Y., Emergent magnetic phase transitions in Fe-doped $SrTiO_{3-\delta}$. *AIP Adv.* **2019**, *9*, 125302.

(24) Fix, T.; Liberati, M.; Aubriet, H.; Sahonta, S.; Bali, R.; Becker, C.; Ruch, D.; MacManus-Driscoll, J.; Arenholz, E.; Blamire, M., Ferromagnetism in Co-doped $(La,Sr)TiO_3$. *New J. Phys.* **2009**, *11*, 073042.

(25) Harrigan, W. L.; Kittilstved, K. R., Reversible modulation of the Cr^{3+} spin dynamics in colloidal $SrTiO_3$ nanocrystals. *J. Phys. Chem. C* **2018**, *122*, 26652-26657.

(26) Harrigan, W. L.; Michaud, S. E.; Lehuta, K. A.; Kittilstved, K. R., Tunable electronic structure and surface defects in chromium-doped colloidal $SrTiO_{3-\delta}$ nanocrystals. *Chem. Mater.* **2016**, *28*, 430-433.

(27) Abdullah, M.; Nelson, R. J.; Kittilstved, K. R., On the formation of superoxide radicals on colloidal $ATiO_3$ (A= Sr and Ba) nanocrystal surfaces. *Nanoscale Adv.* **2020**, *2*, 1949-1955.

(28) Mitchell, R.; Chakhmouradian, A.; Woodward, P., Crystal chemistry of perovskite-type compounds in the tausonite-loparite series,$(Sr_{1-2x}Na_xLa_x)TiO_3$. *Phys. Chem. Miner.* **2000**, *27*, 583-589.
(29) Shannon, R. D., Revised effective ionic radii and systematic studies of interatomic distances in halides and chalcogenides. *Acta Crystallogr.* **1976**, *32*, 751-767.
(30) Drahus, M. D.; Jakes, P.; Erdem, E.; Eichel, R.-A., Defect structure of the mixed ionic electronic conducting $Sr[Ti,Fe]O_x$ solid solution system-change in iron oxidation states and defect complexation. *Solid State Ionics* **2011**, *184*, 47-51.
(31) Noland, J. A., Optical absorption of single-crystal strontium titanate. *Phys. Rev.* **1954**, *94*, 724-724.
(32) Morin, F.; Oliver, J., Energy levels of iron and aluminum in $SrTiO_3$. *Phys. Rev. B* **1973**, *8*, 5847-5854.
(33) Berney, R.; Cowan, D., Photochromism of three photosensitive Fe centers in $SrTiO_3$. *Phys. Rev. B* **1981**, *23*, 37-50.
(34) Leonelli, R.; Brebner, J., Time-resolved spectroscopy of the visible emission band in strontium titanate. *Phys. Rev. B* **1986**, *33*, 8649-8656.
(35) Kan, D. S.; Terashima, T.; Kanda, R.; Masuno, A.; Tanaka, K.; Chu, S. C.; Kan, H.; Ishizumi, A.; Kanemitsu, Y.; Shimakawa, Y.; Takano, M., Blue-light emission at room temperature from Ar^+-irradiated $SrTiO_3$. *Nat. Mater.* **2005**, *4*, 816-819.
(36) Zhang, Q.; Huang, Y.; Peng, S.; Huang, T.; Cao, J.-j.; Ho, W.; Lee, S., Synthesis of $SrFe_xTi_{1-x}O_{3-\delta}$ nanocubes with tunable oxygen vacancies for selective and efficient photocatalytic NO oxidation. *Appl. Catal., B* **2018**, *239*, 1-9.
(37) Muller, K., Paramagnetische Resonanz von Fe^{3+} in $SrTiO_3$-Einkristallen. *Helv. Phys. Acta* **1958**, *31*, 173-204.
(38) Faughnan, B.; Kiss, Z., Optical and EPR studies of photochromic $SrTiO_3$ doped with Fe/Mo and Ni/Mo. *IEEE J. Quantum Electron.* **1969**, *5*, 17-21.
(39) Merkle, R.; Maier, J., Defect association in acceptor-doped $SrTiO_3$: case study for $Fe'_{Ti}V_O$ and $Mn''_{Ti}V^{\bullet\bullet}_O$. *Phys. Chem. Chem. Phys.* **2003**, *5*, 2297-2303.
(40) Lenser, C.; Kalinko, A.; Kuzmin, A.; Berzins, D.; Purans, J.; Szot, K.; Waser, R.; Dittmann, R., Spectroscopic study of the electric field induced valence change of Fe-defect centers in $SrTiO_3$. *Phys. Chem. Chem. Phys.* **2011**, *13*, 20779-20786.
(41) Joost, U.; Šutka, A.; Oja, M.; Smits, K.; Döbelin, N.; Loot, A.; Järvekülg, M.; Hirsimäki, M.; Valden, M.; Nõmmiste, E., Reversible photodoping of TiO_2 nanoparticles for photochromic applications. *Chem. Mater.* **2018**, *30*, 8968-8974.
(42) Dahlman, C. J.; Agrawal, A.; Staller, C. M.; Adair, J.; Milliron, D. J., Anisotropic origins of localized surface plasmon resonance in n-type anatase TiO_2 nanocrystals. *Chem. Mater.* **2019**, *31*, 502-511.
(43) Nisida, Y., Spin-lattice relaxation of Cr^{3+} in coexistence with Ti^{3+} in Al_2O_3. *J. Phys. Soc. Japan* **1965**, *20*, 1390-1399.
(44) Dionne, G. F., Spin-Lattice relaxation of Ti^{3+} ions in $RbAl(SO_4)_2{\cdot}12H_2O$. *Phys. Rev.* **1965**, *139*, A1648.
(45) Brozek, C. K.; Zhou, D.; Liu, H.; Li, X.; Kittilstved, K. R.; Gamelin, D. R., Soluble supercapacitors: large and reversible charge storage in colloidal iron-doped ZnO nanocrystals. *Nano Lett.* **2018**, *18*, 3297-3302.
(46) Zhou, D.; Kittilstved, K. R., Electron trapping on Fe^{3+} sites in photodoped ZnO colloidal nanocrystals. *Chem. Commun.* **2016**, *52*, 9101-9104.
(47) Schrader, M.; Mienert, D.; Oh, T.-S.; Yoo, H.-I.; Becker, K. D., An optical, EPR and electrical conductivity study of blue barium titanate, $BaTiO_{3-\delta}$. *Solid State Sci.* **2008**, *10*, 768-775.
(48) Bersuker, I. B.; Polinger, V., Perovskite Crystals: Unique Pseudo-Jahn–Teller Origin of Ferroelectricity, Multiferroicity, Permittivity, Flexoelectricity, and Polar Nanoregions. *Condens. Matter* **2020**, *5*, 68.
(49) Peper, J. L.; Vinyard, D. J.; Brudvig, G. W.; Mayer, J. M., Slow Equilibration between Spectroscopically Distinct Trap States in Reduced TiO_2 Nanoparticles. *J. Am. Chem. Soc.* **2017**, *139*, 2868-2871.
(50) Suzuki, I.; Gura, L.; Klein, A., The energy level of the $Fe^{2+/3+}$ transition in $BaTiO_3$ and $SrTiO_3$ single crystals. *Phys. Chem. Chem. Phys.* **2019**, *21*, 6238-6246.
(51) Wechsler, B.; Klein, M. B., Thermodynamic point defect model of barium titanate and application to the photorefractive effect. *J. Opt. Soc. Am. B* **1988**, *5*, 1711-1723.
(52) Koehl, A.; Kajewski, D.; Kubacki, J.; Lenser, C.; Dittmann, R.; Meuffels, P.; Szot, K.; Waser, R.; Szade, J., Detection of Fe^{2+} valence states in Fe doped $SrTiO_3$ epitaxial thin films grown by pulsed laser deposition. *Phys. Chem. Chem. Phys.* **2013**, *15*, 8311-8317.
(53) Kubacki, J.; Kajewski, D.; Koehl, A.; Lenser, C.; Dittmann, R.; Szade, J., X-ray absorption and resonant photoemission studies of electroforming process in Fe-doped $SrTiO_3$ epitaxial films. *X-Ray Spectrometry* **2015**, *44*, 339-343.
(54) Comes, R. B.; Kaspar, T. C.; Heald, S. M.; Bowden, M. E.; Chambers, S. A., Infrared optical absorption in low-spin Fe^{2+}-doped $SrTiO_3$. *J. Phys. Cond. Matter* **2016**, *28*, 035901.
(55) Schrauben, J. N.; Hayoun, R.; Valdez, C. N.; Braten, M.; Fridley, L.; Mayer, J. M., Titanium and zinc oxide nanoparticles are proton-coupled electron transfer agents. *Science* **2012**, *336*, 1298-1301.

Table of content graphic

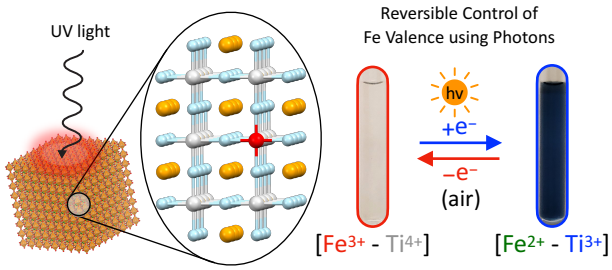

Tunable redox activity at Fe^{3+} centers in colloidal $ATiO_3$ (A = Sr and Ba) nanocrystals

Muhammad Abdullah, Ruby J. Nelson and Kevin R. Kittilstved*

Department of Chemistry, University of Massachusetts Amherst, 710 North Pleasant Street, Amherst, Massachusetts 01003, USA

*Corresponding author: kittilstved@chem.umass.edu

ELECTRONIC SUPPLEMENTARY INFORMATION (ESI):

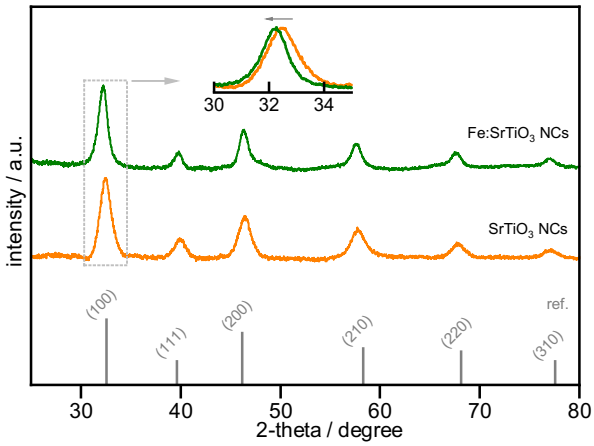

Figure S1. Powder X-ray diffraction pattern of as-prepared $SrTiO_3$ (bottom/black) and Fe:$SrTiO_3$ NCs (top/green) indexed to cubic phase of bulk $SrTiO_3$ with space group of $Pm\bar{3}m$.[1] The baseline was carefully subtracted from both patterns. A slight shift to lower 2θ value in Fe:$SrTiO_3$ NCs displayed in inset is attributed to a typical lattice expansion due to incorporation of relatively larger size Fe^{3+} (0.79 Å) cation at cubic Ti^{4+} (0.75 Å) site.

Table ST1. The average lattice parameter and crystallite size calculated using Rigaku SmartLab Studio II for both samples.

Sample NCs	Lattice parameter (Å)	Crystallite size (nm)†
$SrTiO_3$	3.9197	5.92 ± 0.42
Fe:$SrTiO_3$	3.9256	8.02 ± 0.54

†Crystallite size is the average size calculated from the three most intense reflections: (110), (200) and (211).

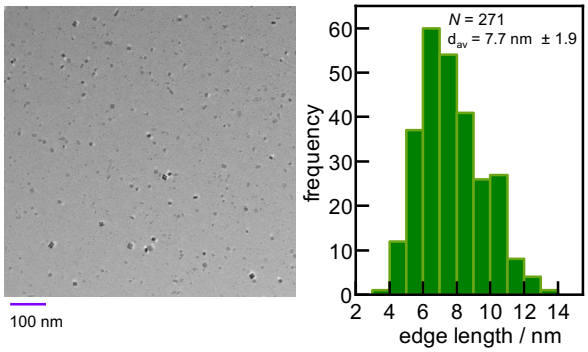

Figure S2. Representative transmission electron microscopy (TEM) image of as-prepared Fe:$SrTiO_3$ NCs deposited on 3 mm copper grid exhibiting a cubic morphology. The size distribution plot from analyzing a few hundred different crystals using ImageJ is shown in the right panel.

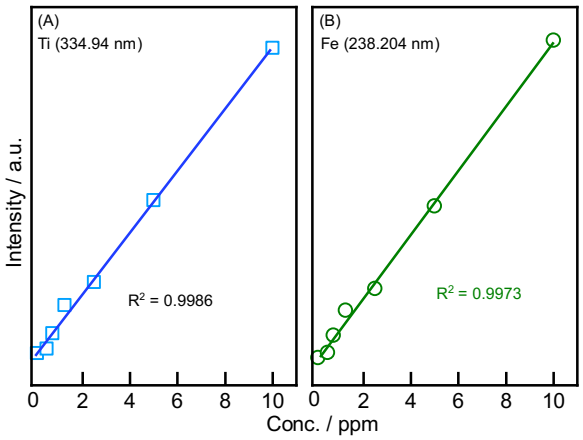

Figure S3. Calibration plots for Ti (left/blue) and Fe (right/green) for ICP-OES measurements using multielement QC-21 Perkin Elmer standard solution to determine percentage in Fe:$SrTiO_3$ NCs. In a typical sample preparation for ICP-OES analysis, solvent-evaporated NCs were digested in aqua regia (~1-2 mL) followed by the dilution in 5% HNO_3 solution.

Table ST2. ICP-OES analysis of Fe content in Fe:$SrTiO_3$ NCs

Sample NCs	Nominal Fe content (%)	Fe from ICP-OES (%)
Fe:$SrTiO_3$	1.0	1.70
Fe:$SrTiO_3$	0.5	1.03

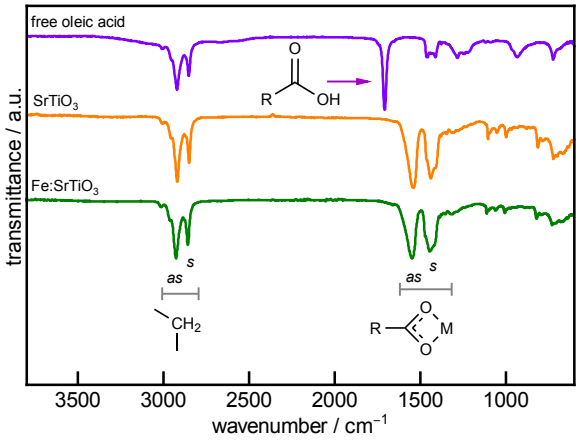

Figure S4. FTIR spectra of solvent evaporated $SrTiO_3$ (orange) and Fe:$SrTiO_3$ (green) NCs. The top purple spectrum belongs to free oleic acid. The pair of peaks at 1450 cm^{-1} and 1550 cm^{-1} corresponding to the symmetric (*s*) and asymmetric (*as*) stretches of bound carboxylate head group of oleate ligand is observed in both NCs. Aliphatic bands of oleate ligands are also present *ca.* 2900 cm^{-1}, which indicate the NCs surfaces are passivated by oleate ligands

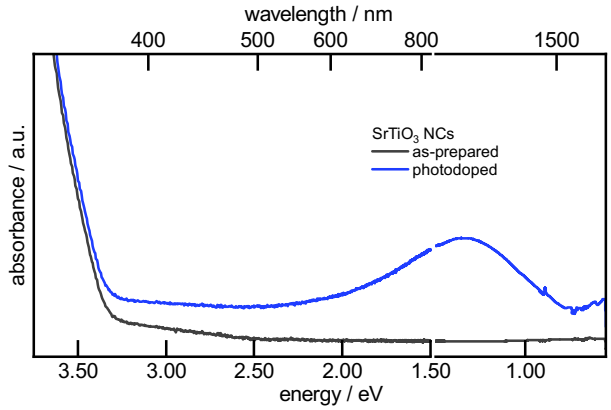

Figure S5. Electronic absorption spectrum of as-prepared and photodoped $SrTiO_3$ NCs. The full spectrum was made by splicing the spectra collected on a Cary 50 for $\lambda < 900$ nm and a Varian 670 for $\lambda > 900$ nm.

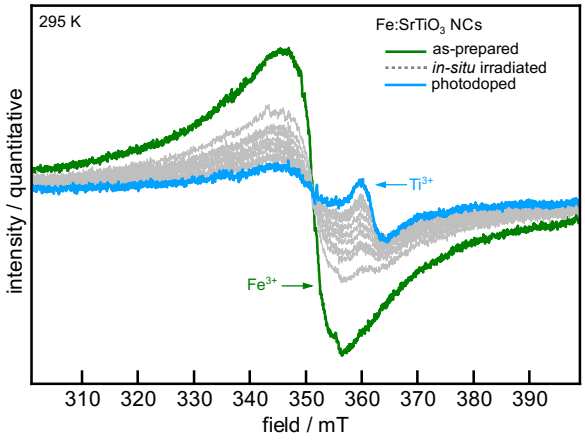

Figure S6. Room temperature in situ EPR spectra of $Fe:SrTiO_3$ NCs as a function of photodoping time. The green spectrum belongs to as-prepared NCs before turning on the Xe lamp. After turning on the lamp, the broad Fe^{3+} signal decreases in intensity and linewidth while a new feature at ~360 mT appears (grey lines). This new signal is assigned to Ti^{3+} defects. The blue spectrum shows the photodoped NCs with some residual Fe^{3+} signal which can be completely eliminated upon prolonged photodoping as discussed in the main paper.

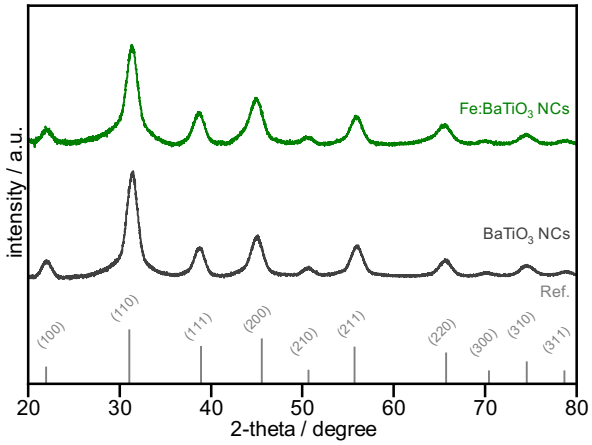

Figure S7. Powder X-ray diffraction pattern of as-prepared $BaTiO_3$ (bottom/black) and $Fe:BaTiO_3$ NCs (top/green) indexed to cubic phase of bulk $BaTiO_3$ with space group of $Pm\bar{3}m$.[2] The average particle size calculated from peak analysis is shown below.

Table ST3. The average lattice parameter and crystallite size calculated using Rigaku SmartLab Studio II for both samples.

Sample NCs	Lattice parameter (Å)	Crystallite size (nm)†
$BaTiO_3$	4.0230	6.10 ± 0.4
Fe-doped $BaTiO_3$	4.0523	5.04 ± 0.9

†Crystallite size is the average size calculated from the three most intense reflections: (110), (200) and (211).

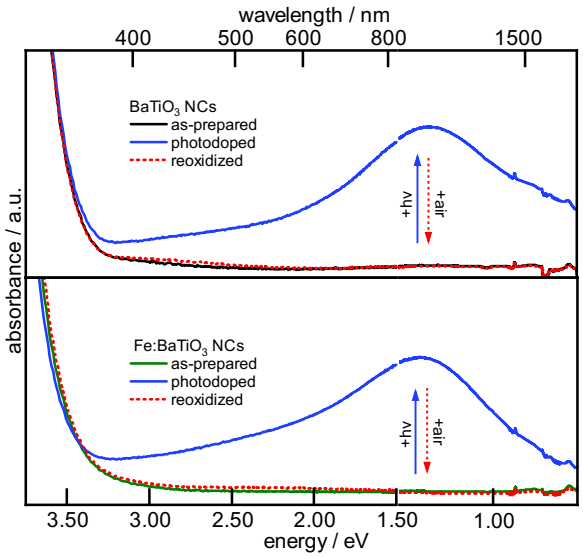

Figure S8. Electronic absorption spectra of an air-free solution of $BaTiO_3$ and Fe:$BaTiO_3$ NCs in hexanes before and after photodoping.

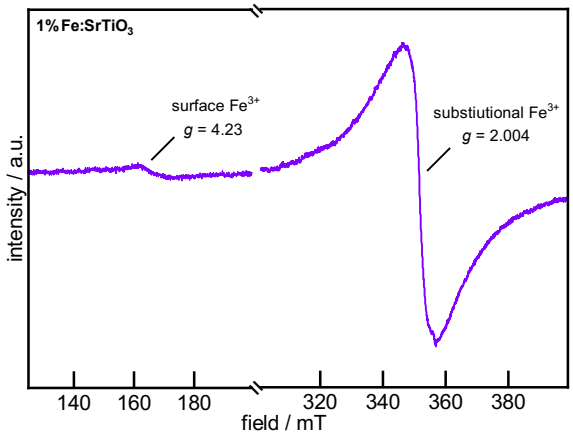

Figure S9. Room temperature EPR spectrum of nominally 1% Fe-doped $SrTiO_3$ NCs.

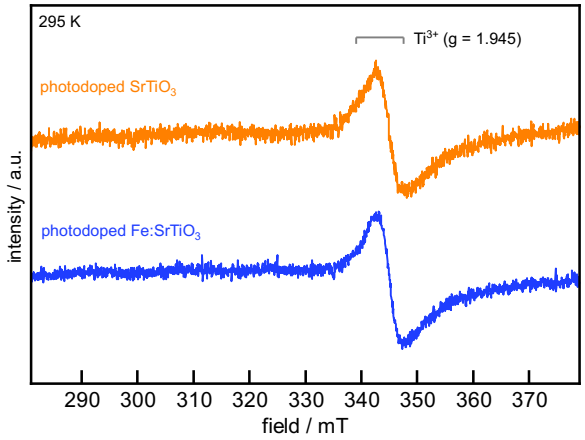

Figure S10. The CW-EPR spectra of collected at room temperature of maximally photodoped $SrTiO_3$ (top/orange) and Fe:$SrTiO_3$ NCs (bottom/blue) displaying the characteristics resonance at $g = 1.945$ attributed to Ti^{3+} defects. The concentration of NCs in each sample was kept the same, approximated from the combination of ICP-EOS and particle size analysis.

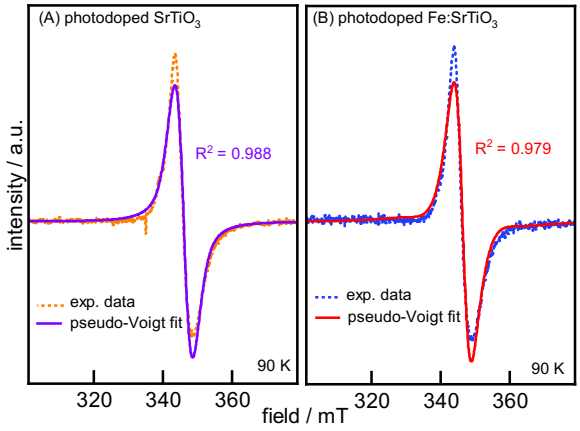

Figure S11. CW-EPR spectra collected well below the saturation power at 90 K of (A) photodoped $SrTiO_3$ and (B) photodoped Fe:$SrTiO_3$ NCs. The purple and red lines are best fits to pseudo-Voigt line profile to obtain the Lorentzian width (Γ_L) to calculate the spin-spin relaxation time (T_2) using equation 1.

$$T_2 = 2/(\gamma_e \Gamma_L) \qquad \text{(eq. 1)}$$

Where γ is the electron gyromagnetic ratio ($1.760859708 \times 10^{11}\ s^{-1}T^{-1}$).

Equation 2 shown below was used to fit the power saturation data shown in Figures 4A-C in the main text to determine the term P_2 which is the product of the spin-lattice ($1/T_1$) and spin-spin relaxation rate ($1/T_2$) as shown in equation 3. Where c is a scaler and ε is a measure of line homogeneity.

$$\Delta Y = c \cdot h_1 \left(1 + \frac{(h_1)^2}{P_2}\right)^{-\varepsilon} \qquad \text{(eq. 2)}$$

$$P_2 = (\gamma_e^2 T_1 T_2)^{-1} \qquad \text{(eq. 3)}$$

Table ST4. Spin-spin relaxation time (T_2) calculated from Lorentzian width (Γ_L) from fitting EPR spectra of both samples to first derivative pseudo-Voigt line profile as displayed in figure S10.

Sample NCs	Γ_L (G)	T_2 (ns)
$SrTiO_3$	42.88 ± 1.11	2.65 ± 0.06
Fe:$SrTiO_3$	45.75 ± 0.62	2.50 ± 0.04

REFERENCES:

(1) Mitchell, R.; Chakhmouradian, A.; Woodward, P. Crystal chemistry of perovskite-type compounds in the tausonite-loparite series, $(Sr_{1-2x}Na_xLa_x)TiO_3$. *Phys. Chem. Miner.* **2000,** *27*(8), 583-589.
(2) Kwei, G.; Lawson, A.; Billinge, S.; Cheong, S.-W. Structures of the ferroelectric phases of barium titanate. *J. Phys. Chem.* **1993,** *97*(10), 2368-2377.